
K-BAND: SELF-SUPERVISED MRI RECONSTRUCTION VIA STOCHASTIC GRADIENT DESCENT OVER k -SPACE SUBSETS

A PREPRINT

Frederic Wang, Han Qi, Alfredo De Goyeneche, Reinhard Heckel, Michael Lustig, and Efrat Shimron

August 8, 2023

ABSTRACT

Although deep learning (DL) methods are powerful for solving inverse problems, their reliance on high-quality training data is a major hurdle. This is significant in high-dimensional (dynamic/volumetric) magnetic resonance imaging (MRI), where acquisition of high-resolution fully sampled k -space data is impractical. We introduce a novel mathematical framework, dubbed *k-band*, that enables training DL models using only partial, limited-resolution k -space data. Specifically, we introduce training with *stochastic gradient descent (SGD) over k -space subsets*. In each training iteration, rather than using the fully sampled k -space for computing gradients, we use only a small k -space portion. This concept is compatible with different sampling strategies; here we demonstrate the method for k -space “bands”, which have limited resolution in one dimension and can hence be acquired rapidly. We prove analytically that our method stochastically approximates the gradients computed in a fully-supervised setup, when two simple conditions are met: (i) the limited-resolution axis is chosen randomly-uniformly for every new scan, hence k -space is fully covered across the entire training set, and (ii) the loss function is weighed with a mask, derived here analytically, which facilitates accurate reconstruction of high-resolution details. Numerical experiments with raw MRI data indicate that *k-band* outperforms two other methods trained on limited-resolution data and performs comparably to state-of-the-art (SoTA) methods trained on high-resolution data. *k-band* hence obtains SoTA performance, with the advantage of training using only limited-resolution data. This work hence introduces a practical, easy-to-implement, self-supervised training framework, which involves fast acquisition and self-supervised reconstruction and offers theoretical guarantees.

1 Introduction

The last decade has seen an unprecedented rise of Deep Learning (DL) techniques in various research fields, including computational Magnetic Resonance Imaging (MRI). Although MRI produces high-quality images with diverse contrasts, its clinical application is restricted by its long acquisition time, which causes limited spatio-temporal resolution and sensitivity to motion artifacts. To tackle this challenge, extensive research efforts have been devoted to accelerating MRI scans, primarily through k -space (Fourier-domain) undersampling and the development of image reconstruction algorithms that can infer the missing information. Well-established approaches include Parallel Imaging (PI) with multi-coil arrays [1–5], and Compressed Sensing (CS), which involves random undersampling and transform-domain regularization [6–12]. The latter can be learned using DL [13–26].

Frederic Wang and Han Qi contributed equally to this work. The authors would like to acknowledge funding from grants U24EB029240, U01EB029427, R01EB009690, GE Healthcare. E.S. acknowledges funding from the Weizmann Institute Women’s Postdoctoral Career Development Award in Science. (*Corresponding author: Efrat Shimron*).

F.W., H.Q., A.D.G., M.L., E.S., are affiliated with the Department of Electrical Engineering and Computer Sciences, University of California, Berkeley, Berkeley, CA 94720 USA. E-mails: fredwang@berkeley.edu, han2019@berkeley.edu, adg@berkeley.edu, mlustig@eecs.berkeley.edu, efrat.s@berkeley.edu

R.H. is affiliated with the Department of Computer Engineering, Technical University of Munich, Munich, Germany, 80333 (e-mail: reinhard.heckel@tum.de).

Nevertheless, a critical challenge that hinders the development of DL methods is the need for high-quality training data. Open-access databases of raw, high-quality MRI measurements are available but scarce, and offer only limited types of data [27–30]. Other databases offer non-raw MR images, but these are often preprocessed and hence could lead to biased results [31]. Researchers thus often need to create new training databases from scratch, a task that is highly challenging due to the slow MRI acquisition rate. These challenges are significant in high-dimensional dynamic MRI, where it is often impractical to acquire full k -space data and there is an inherent tradeoff between the spatial and temporal resolutions [15, 17, 32]. This is a barrier for development of techniques for applications such as pulmonary [33], flow [34], and dynamic contrast-enhanced imaging [35, 36].

There is hence a growing interest in the development of self-supervised techniques, which enable training networks using only partial k -space data [16, 17, 37]. Recent methods include, for example, the Self-Supervised learning via Data Undersampling (SSDU) [38] method that splits the undersampled measurements into two disjoint sets, a collaborative learning method, where two networks are trained in parallel using different k -space subsets [39], zero-shot learning methods [40, 41], Deep Image Prior methods [42–45], and methods based on generative adversarial networks (GANs) [46]. Although each of these self-supervised methods is meritorious, they are sometimes difficult to implement in practice.

Here we introduce a mathematical framework, dubbed “ k -band”, that enables training DL models in a self-supervised manner using only partial, limited-resolution k -space data. Specifically, we introduce training with *stochastic gradient descent (SGD) over k -space subsets*. Rather than using the entire k -space to compute the gradients, we propose to use only a small, contiguous k -space portion. While our approach generalizes to various sampling strategies, here we focus on acquisition of k -space “bands”, which are fast, simple to implement, and highly suitable for high-dimensional MRI. We derive the proposed training method analytically and show that it stochastically approximates fully supervised SGD training with full k -space data. We also demonstrate it through extensive numerical experiments with raw MRI data. In summary, this paper introduces a practical, easy-to-implement framework, which involves fast acquisition and self-supervised reconstruction and offers theoretical guarantees.

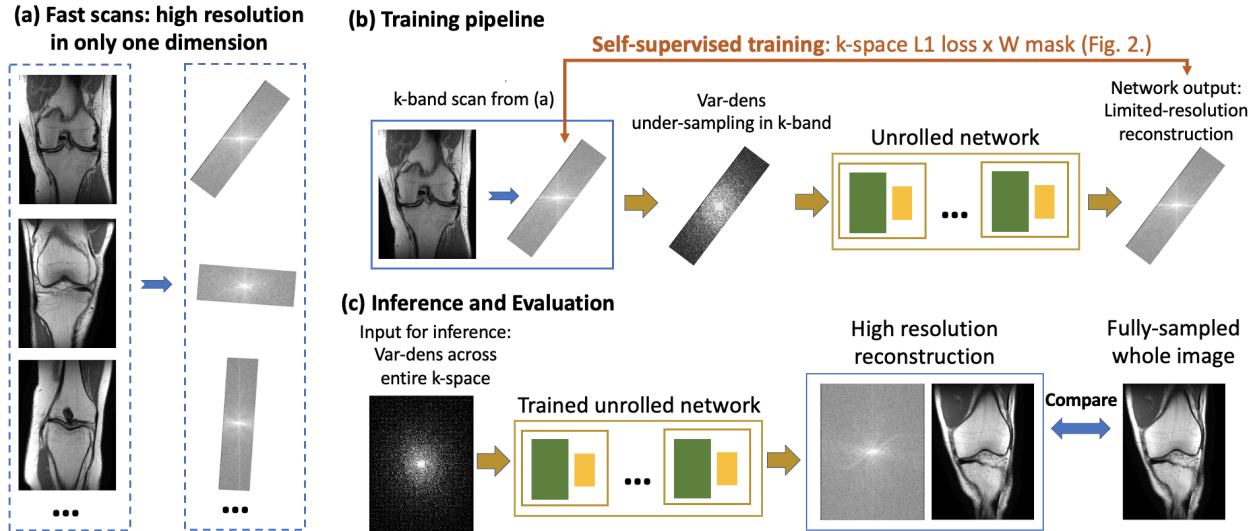


Figure 1: The proposed k -band strategy. (a) Training data consists of k -space bands, with different orientations across training examples. (b) During training, the band is undersampled with a variable-density mask and the network learns to reconstruct images through self-supervision. (c) During inference, the network is not limited to low-resolution data. It receives variable-density undersampled data from the entire k -space, and reconstructs high-resolution images even though it never saw such examples during training.

2 Background: The MRI inverse problem

This work addresses the problem of image reconstruction from sub-Nyquist sampled k -space (Fourier domain) measurements. The aim is to reconstruct an image \mathbf{x} from the noisy, under-sampled measurements $\mathbf{y} = \mathbf{M}\mathbf{F}\mathbf{x} + \mathbf{e}$, where \mathbf{F} is an operator that describes the imaging system (the Fourier transform), \mathbf{M} is an operator that chooses the locations of the sampled k -space pixels, and \mathbf{e} is noise. For simplicity, we describe the method here for a single-coil scenario; the extension to multi-coil data is straightforward, as the \mathbf{F} operator can also include the coils’ sensitivity maps.

A common approach to reconstruct the image from the measurements is to solve the regularized least-squares problem

$$\operatorname{argmin}_{\mathbf{x}} \|\mathbf{M}\mathbf{F}\mathbf{x} - \mathbf{y}\|_2^2 + R(\mathbf{x}) \tag{1}$$

where $R(\mathbf{x})$ is a regularizer, which is often a sparsity-promoting ℓ_1 penalty [6]. In DL frameworks, the reconstruction problem is commonly solved by training a neural network f_{θ} with parameters θ to map the measurements to a clean image. The network is typically trained in a supervised fashion, by minimizing a loss such as

$$L(\theta) = \frac{1}{N} \sum_{i=1}^N \operatorname{loss}(\mathbf{x}_i, f_{\theta}(\mathbf{y}_i)) \tag{2}$$

where the loss function can be the mean-squared error, for example. The training process hence requires pairs of measurements and target images.

The network architecture has substantial influence on the overall performance. At present, an architecture termed "unrolled neural networks" gives state-of-the-art (SoTA) performance [47]. This architecture is obtained by unrolling the iterations of the regularized least-squares objective (eq. (1)) with a first-order optimization algorithm. For example, gradient descent applied to this objective gives the iterates

$$\mathbf{x}_{k+1} = \mathbf{x}_k - \alpha_k \left(\frac{1}{2} \mathbf{y}^T (\mathbf{M}\mathbf{F}\mathbf{x}_k - \mathbf{y}) + \nabla R(\mathbf{x}_k) \right) \tag{3}$$

where α_k is the step size (learning rate). In those iterates the gradient of the regularizer (i.e., $\nabla R(\mathbf{x}_k)$) is parameterized with a neural network (for example a U-net), which yields an unrolled neural network f_{θ} . The latter takes the measurement \mathbf{y} as input and outputs an estimate of the image. In this architecture, the forward model is known, not learned. There are different methods for unrolling the iterates (with different first-order-gradient methods) and for parameterizing the regularizer gradient; for a review see [17]. In this work we follow the MoDL formulation [24]. However, in contrast to MoDL, which is fully supervised, we develop a framework that enables training using only partial *k*-space data.

3 Method and theory

This work is motivated by the practical limitations in MRI, where data must be acquired rapidly and full *k*-space sampling is often impossible. In applications where the acquisition window is short (e.g. dynamic contrast-enhanced MRI), only a small portion of *k*-space can be acquired with high resolution. To address this challenge we re-design the acquisition and training strategies synergistically. We introduce the *k*-band framework, which enables end-to-end self-supervised training of neural networks using only *limited-resolution data*.

3.1 *k*-band overview

Proposed approach: SGD over *k*-space subsets. We start from the well-established SGD training method, which minimizes the fully-supervised loss (eq. (2)), and breaks down the gradient computation into smaller steps. In every iteration of the standard SGD, an example $(\mathbf{x}_i, \mathbf{y}_i)$ (or a mini-batch of examples) is chosen stochastically from the training set, and the gradient $\nabla \operatorname{loss}(\mathbf{x}_i, f_{\theta}(\mathbf{y}_i))$ is computed using its *fully sampled k-space*. Instead, we propose to approximate the gradient computation using only a portion of the *k*-space data. Our training method, termed *SGD over k-space subsets*, is derived analytically in the next section. Here we start with an overview of our framework.

Acquisition strategy. The proposed *SGD over k-space subsets* is general and can be applied to different acquisition schemes. Here we propose to collect training data by acquiring *k*-space "bands", which have high resolution along the readout dimension and limited resolution along the phase-encoding (PE) dimension (Fig. 1a). From here on we refer to data acquired in such bands as "limited-resolution data".

We chose this acquisition scheme because it offers several important advantages. First, it is highly suitable for fast acquisition. As only a portion of *k*-space is sampled, bands can be acquired rapidly and repeatedly. This may allow increasing the temporal resolution in dynamic scans or faster volume coverage in high-dimensional scans. Secondly, bands can be acquired easily using any commercial MRI scanner without changing the pulse sequence, by changing only two parameters, the PE resolution and scan orientation. Third, because the data within each band are fully sampled, this acquisition yields images that exhibit local blurring and ringing but are *free of global streaking or aliasing artifacts*. Such images may hence be more suitable for training DL models compared with images obtained from scattered sampling, e.g. variable-density (VD) sampling. Finally, because the proposed acquisition is rapid, it can

be used to fill dead-time between scans in an MRI exam session and hence be easily integrated in a clinical workflow to obtain new datasets.

Self-supervised training. In every training iteration, one example is chosen at random and its band is retrospectively undersampled using a VD scheme. This scheme was chosen because it generates incoherent artifacts that are highly suitable for removal in optimization-based reconstruction [6]. Notice that because the VD undersampling is implemented retrospectively, it does not affect the data acquisition benefits discussed above. The input to the network is the VD-undersampled band, and the training target is the entire band (Fig. 1b).

We compute the loss in k -space, only inside the bands. Note that *all the data within the band* is used for supervision, and there is *no supervision* outside the band. We chose to avoid regularization outside the band to allow the network to learn priors for the entire k -space. Importantly, even though every band covers only a small region of k -space, across the training session all of k -space is covered as the training examples should ideally have different orientations in k -space; this condition emerges from the analytical derivation described below.

Inference. The test data are acquired using a VD undersampling mask that covers the entire k -space, with the same VD statistics as during training. Inference is done using the pre-trained network without any re-training. Note that even though the network was trained using limited-resolution examples (k -space bands), during test time it must generalize to high-resolution reconstructions. This work aims to show that the proposed k -band framework enables this test-time generalization.

3.2 k -band proof

Here we derive the proposed *SGD over k -space subsets* method analytically and find the conditions under which it stochastically approximates fully supervised SGD, i.e. training with fully sampled k -space data.

Supervised training with a loss L applied in the Fourier domain minimizes an empirical version of the risk

$$R(\boldsymbol{\theta}) = \mathbb{E} [L(\mathbf{F}f_{\boldsymbol{\theta}}(\mathbf{y}) - \mathbf{F}\mathbf{x})]. \tag{4}$$

Here, the expectation is over a joint distribution over the image \mathbf{x} and corresponding measurement \mathbf{y} . Suppose the loss L is of the form $L(\mathbf{z}) = \sum_j \ell([\mathbf{z}]_j)$ where $\ell: \mathbb{C} \rightarrow \mathbb{R}$ is a scalar function obeying $\ell(0) = 0$ and $[\mathbf{z}]_j$ represents pixel j of the flattened image x . Let us define \mathbf{U} as a stochastic mask sampled independently of (\mathbf{x}, \mathbf{y}) , and the corresponding weighted loss as $L^W(\mathbf{z}) = \sum_j \mathbf{W}_{jj} \ell([\mathbf{z}]_j)$ where \mathbf{W} is a deterministic weighting mask. A weighted stochastic gradient resulting from this loss can be written as

$$G(\boldsymbol{\theta}) = \nabla_{\boldsymbol{\theta}} L^W(\mathbf{U}(\mathbf{F}f_{\boldsymbol{\theta}}(\mathbf{y}) - \mathbf{F}\mathbf{x})). \tag{5}$$

Note that computation of the gradient doesn't require knowledge of the image \mathbf{x} , an undersampled measurement $\mathbf{U}\mathbf{F}\mathbf{x}$ is sufficient.

Proposition 3.1. *Suppose that the matrix \mathbf{W} is a deterministic diagonal matrix obeying*

$$\mathbf{W}_{jj} = \frac{1}{\mathbb{E}[\mathbf{U}_{jj}]} \tag{6}$$

$$\Leftrightarrow \mathbf{W} = (\mathbb{E}[\mathbf{U}])^{-1}. \tag{7}$$

Then

$$\mathbb{E}_{\mathbf{x}, \mathbf{y}, \mathbf{U}} [G(\boldsymbol{\theta})] = \nabla R(\boldsymbol{\theta}). \tag{8}$$

The proposition states that *SGD over k -space subsets* enables us to compute unbiased stochastic gradients of the risk. Thus, with sufficient training data, the proposed training yields a network as good as one trained in a fully supervised fashion.

Proof. The expectation of the stochastic gradient is

$$\begin{aligned}
\mathbb{E}[G(\boldsymbol{\theta})] &= \nabla_{\boldsymbol{\theta}} \mathbb{E}_{(\mathbf{x}, \mathbf{y}), \mathbf{U}} [L^W(\mathbf{U}(\mathbf{F}f_{\boldsymbol{\theta}}(\mathbf{y}) - \mathbf{F}\mathbf{x}))] \\
&\stackrel{i}{=} \nabla_{\boldsymbol{\theta}} \mathbb{E}_{(\mathbf{x}, \mathbf{y}), \mathbf{U}} \left[\sum_j \mathbf{W}_{jj} \ell(\mathbf{U}_{jj}[\mathbf{F}f_{\boldsymbol{\theta}}(\mathbf{y}) - \mathbf{F}\mathbf{x}]_j) \right] \\
&\stackrel{ii}{=} \nabla_{\boldsymbol{\theta}} \mathbb{E}_{(\mathbf{x}, \mathbf{y}), \mathbf{U}} \left[\sum_j \mathbf{W}_{jj} \mathbf{U}_{jj} \ell([\mathbf{F}f_{\boldsymbol{\theta}}(\mathbf{y}) - \mathbf{F}\mathbf{x}]_j) \right] \\
&\stackrel{iii}{=} \nabla_{\boldsymbol{\theta}} \mathbb{E}_{(\mathbf{x}, \mathbf{y})} \left[\sum_j \mathbf{W}_{jj} \mathbb{E}_{\mathbf{U}} [\mathbf{U}_{jj}] \ell([\mathbf{F}f_{\boldsymbol{\theta}}(\mathbf{y}) - \mathbf{F}\mathbf{x}]_j) \right] \\
&\stackrel{iv}{=} \nabla_{\boldsymbol{\theta}} \mathbb{E}_{(\mathbf{x}, \mathbf{y})} \left[\sum_j \ell([\mathbf{F}f_{\boldsymbol{\theta}}(\mathbf{y}) - \mathbf{F}\mathbf{x}]_j) \right] \\
&= \nabla_{\boldsymbol{\theta}} R(\boldsymbol{\theta}),
\end{aligned}$$

as desired. Equation (i) uses the definition on the loss L , equation (ii) uses the fact that $U_{jj} \in \{0, 1\}$ and $\ell(0) = 0$, equation (iii) uses the independence of \mathbf{U} and (\mathbf{x}, \mathbf{y}) , and equation (iv) uses the assumption on the masks. \square

Corollary 3.1. *Let \mathbf{B}_i represent the band-acquisition mask of angle $i \in \{1, \dots, 180\}$. K -band stochastically approximates fully supervised training with element-wise Fourier domain loss weighting when*

$$\mathbf{W} = 180 \left(\sum_{i=1}^{180} \mathbf{B}_i \right)^{-1} \quad (9)$$

Proof. We can express the k -band training gradient using the stochastic gradient formulation. Suppose we acquire k -space with band mask \mathbf{B}_i , and suppose \mathbf{V} is an arbitrary variable-density undersampling mask. Then the k -band training loss can be written as

$$L^W(\mathbf{B}_i(\mathbf{F}f_{\boldsymbol{\theta}}(\mathbf{B}_i \mathbf{V} \mathbf{F} \mathbf{x}) - \mathbf{F} \mathbf{x})) \quad (10)$$

By Proposition II.1, we can approximate fully-supervised training by weighting the loss of k -band element-wise in the Fourier domain with

$$\mathbf{W} = (\mathbb{E}[\mathbf{U}])^{-1} = \left(\frac{1}{\mathbb{E}[\mathbf{B}_i]} \right)^{-1} = 180 \left(\sum_{i=1}^{180} \mathbf{B}_i \right)^{-1} \quad (11)$$

where the last step is because each band mask \mathbf{B}_i is sampled uniformly from all possible orientations. \square

Corollary 3.2. *Both ℓ_1 and ℓ_2 loss functions (in k -space) satisfy the conditions for L .*

Proof. Using our definition of $L(\mathbf{z}) = \sum_j \ell(\mathbf{z}_j)$, ℓ_1 loss can be defined with $\ell(x) = |x|$ which satisfies $\ell(0) = |0| = 0$. Additionally, ℓ_2 loss can be defined with $\ell(x) = \|x\|_2^2$, which satisfies $\ell(0) = \|0\|_2^2 = 0$. \square

Remarks: Suppose we use the squared- ℓ_2 loss, i.e., $L(\mathbf{z}) = \|\mathbf{z}\|_2^2$. Then by Parseval's Theorem, we have that training in the Fourier domain is equivalent to training in the image domain, as follows:

$$R(\boldsymbol{\theta}) = \mathbb{E} \left[\|\mathbf{F}f_{\boldsymbol{\theta}}(\mathbf{y}) - \mathbf{F}\mathbf{x}\|_2^2 \right] = \mathbb{E} \left[\|f_{\boldsymbol{\theta}}(\mathbf{y}) - \mathbf{x}\|_2^2 \right].$$

It is also important to choose stochastic gradients that have a small variance, since stochastic gradients with a smaller variance result in stochastic gradient converging faster and thus requiring fewer training examples. See [48, Appendix B] for a precise statement.

Proposition 3.2. *Suppose that $\|\nabla_{\theta} f_{\theta}(\mathbf{y})\|_2^2 \leq M$, i.e. the network is M -Lipschitz, and suppose that $|\nabla_x l(x)| \leq D$, i.e. the loss function is D -Lipschitz. Let $C = \max_j(\mathbf{W}_{jj})$. We have*

$$\mathbb{E}_{\mathbf{x}, \mathbf{y}, \mathbf{U}} [\|G(\theta)\|^2] \leq CD^2M$$

Proof. Let $\mathbf{z} = \mathbf{F}f_{\theta}(\mathbf{y}) - \mathbf{F}\mathbf{x}$ for simplicity. We have

$$\begin{aligned} \mathbb{E}_{(\mathbf{x}, \mathbf{y}), \mathbf{U}} [\|G(\theta)\|^2] &= \mathbb{E}_{(\mathbf{x}, \mathbf{y}), \mathbf{U}} [\|\nabla_{\theta} L^W(\mathbf{U}\mathbf{z})\|^2] \\ &= \mathbb{E}_{(\mathbf{x}, \mathbf{y}), \mathbf{U}} \left[\left(\sum_i \mathbf{W}_{ii} \mathbf{U}_{ii} \nabla_{\theta} \ell([\mathbf{z}]_i) \right)^2 \right] \\ &= \mathbb{E}_{(\mathbf{x}, \mathbf{y}), \mathbf{U}} \left[\sum_i \sum_j \mathbf{W}_{ii} \mathbf{U}_{ii} \mathbf{W}_{jj} \mathbf{U}_{jj} \nabla_{\theta} \ell([\mathbf{z}]_i) \nabla_{\theta} \ell([\mathbf{z}]_j) \right] \\ &\stackrel{i}{=} \mathbb{E}_{(\mathbf{x}, \mathbf{y}), \mathbf{U}} \left[\sum_i \mathbf{W}_{ii}^2 \mathbf{U}_{ii}^2 (\nabla_{\theta} \ell([\mathbf{z}]_i))^2 \right] \\ &\stackrel{ii}{=} \mathbb{E}_{(\mathbf{x}, \mathbf{y})} \left[\sum_i \mathbf{W}_{ii} (\nabla_{\theta} \ell([\mathbf{z}]_i))^2 \right] \\ &= \mathbb{E}_{(\mathbf{x}, \mathbf{y})} \left[\sum_i \mathbf{W}_{ii} (\nabla_{\theta} \ell([\mathbf{F}f_{\theta}(\mathbf{y}) - \mathbf{F}\mathbf{x}]_i))^2 \right] \\ &\stackrel{iii}{=} \mathbb{E}_{(\mathbf{x}, \mathbf{y})} \left[\sum_i \mathbf{W}_{ii} (\ell'([\mathbf{F}f_{\theta}(\mathbf{y}) - \mathbf{F}\mathbf{x}]_i) [\mathbf{F}\nabla_{\theta} f_{\theta}(\mathbf{y})]_i)^2 \right] \\ &\stackrel{iv}{\leq} D^2 \mathbb{E}_{(\mathbf{x}, \mathbf{y})} \left[\sum_i \mathbf{W}_{ii} [\mathbf{F}\nabla_{\theta} f_{\theta}(\mathbf{y})]_i^2 \right] \\ &\stackrel{v}{\leq} CD^2 \mathbb{E}_{(\mathbf{x}, \mathbf{y})} [\|\mathbf{F}\nabla_{\theta} f_{\theta}(\mathbf{y})\|_2^2] \\ &\stackrel{vi}{=} CD^2 \mathbb{E}_{(\mathbf{x}, \mathbf{y})} [\|\nabla_{\theta} f_{\theta}(\mathbf{y})\|_2^2] \\ &\stackrel{vii}{\leq} CD^2M \end{aligned}$$

as desired. Equation (i) comes from the fact that $\mathbb{E}[\mathbf{W}_{ii}\mathbf{U}_{ii}] = \mathbb{E}[\mathbf{W}_{jj}\mathbf{U}_{jj}] = 1$ and that those terms are independent for $i \neq j$, leaving only the diagonal squared terms after simplification. Equation (ii) uses the fact that $\mathbf{U}_{ii} \in \{0, 1\}$, so $\mathbb{E}[\mathbf{U}_{ii}^2] = 0^2\mathbb{P}(\mathbf{U}_{ii} = 0) + 1^2\mathbb{P}(\mathbf{U}_{ii} = 1) = \mathbb{E}[\mathbf{U}_{ii}] = \mathbf{W}_{ii}^{-1} = \mathbb{E}[\mathbf{W}_{ii}^{-1}]$. Equation (iii) uses the chain rule, equation (iv) uses our assumption on the Lipschitz condition on the loss, equation (v) comes from our assumption on the maximum value of \mathbf{W} , equation (vi) comes from Parseval's Theorem, and equation (vii) comes from our assumption of the Lipschitz condition of the neural network. \square

Corollary 3.3. *By using a loss function with a bounded gradient, there will be smaller variance in gradients especially during early stages of training when the residuals are high. This choice allows for better convergence to the optimal fully-supervised network weights and thus better network generalization to high-resolution inputs. Under this regime, ℓ_1 loss ($D = |\ell_1(x)| = 1$) is expected to perform better than ℓ_2 loss ($D = |\ell_2(x)| = |x|$).*

Summary. We find that the proposed method stochastically approximates training with SGD on fully-sampled high-resolution data when the following conditions are met: (i) the limited-resolution axis is chosen randomly-uniformly for every new scan, hence k -space is fully covered across the entire training set. (ii) The k -space loss function is multiplied by the deterministic weighting mask \mathbf{W} from equation (9), which facilitates accurate reconstruction of high-resolution details. We also show that training k -band using a loss function in k -space with a small gradient, i.e. ℓ_1 loss, allows better approximation of fully supervised training compared with ℓ_2 loss.

Example of a \mathbf{W} mask. Generally, different \mathbf{W} masks should be computed for acquisitions with different band widths, as the values of the mask depend on the band shape. Fig. 2 shows an example for a band that covers 33% of k -space. As can be seen, the mask has a spatial structure that gives more weight towards peripheral k -space areas.

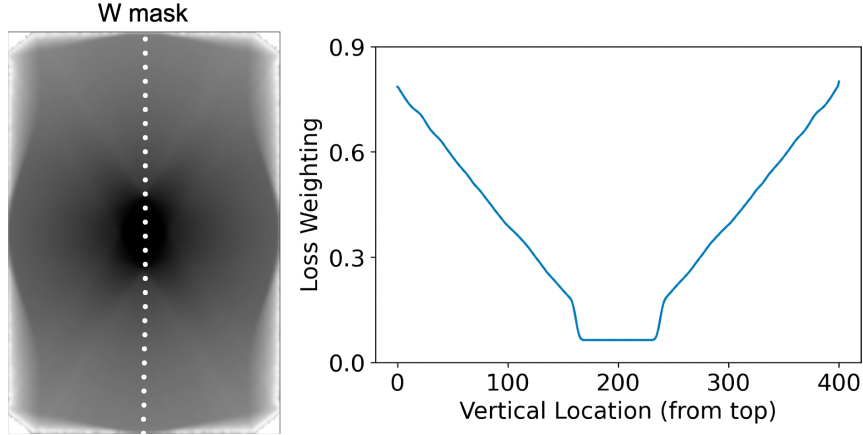


Figure 2: (Left) Example loss-weighting (W) mask for a band area of 33%, shown in logarithm scale for structure. (Right) Vertical profile for W mask column displayed in white on the left.

3.3 The k -band training method

In the k -band framework, we use an ℓ_1 k -space loss, with supervision only within the band. Our choice of this loss is motivated by Corollary 3.3 and by our numerical observation that it gives better results than other loss functions, as described in the Results section. We train the network using an unrolled optimization scheme formulated by,

$$\mathbf{x}_{n+1} = (\mathbf{F}^H \mathbf{B}^H \mathbf{B} \mathbf{F} + \eta \mathbf{I})^{-1} ((\mathbf{B} \mathbf{F})^H \mathbf{y} + \eta \mathbf{z}_n) \quad (12)$$

$$\mathbf{z}_n = \text{CNN}_\theta(\mathbf{x}_n) \quad (13)$$

where H is the Hermitian transpose, η is a regularization parameter, \mathbf{W} is the loss weighting derived above (see eq. (9)) and $\mathbf{B} \in \{\mathbf{B}_i\}_{i=1, \dots, 180}$ is a band sampling operator (see Corollary 3.1). Here, CNN_θ describes the network contained within one block (one iterate) of the unrolled network f_θ .

The network is trained end-to-end and the loss is computed using the output of the last network layer, as in [24]. However, in contrast to the (unweighted) image-domain loss of [24], here the network is trained using the proposed weighted ℓ_1 k -space loss, formulated by,

$$L(\theta) = \frac{1}{N} \sum_{i=1}^N \|\mathbf{W} \mathbf{B}^{(i)} (\mathbf{F} f_\theta(\mathbf{y}^{(i)}) - \mathbf{F} \mathbf{x}^{(i)})\|_1 \quad (14)$$

where $\mathbf{x}^{(i)}$ are the band-limited k -space data of sample i , $\mathbf{y}^{(i)}$ are the corresponding VD-undersampling input, and $\mathbf{B}^{(i)}$ is the binary band mask.

4 Experiments

This section describes the experiments that were conducted to demonstrate k -band numerically.

4.1 Data

Experiments were performed using raw multi-coil knee and brain data from fastMRI [27]. Specifically, we used proton-density fat-saturated knee data, and T1-weighted, T2-weighted and FLAIR brain data. Each scan contains 20-30 slices. We used only the 10 middle slices from each scan (where structure is abundant), and normalized the intensity of each slice to its 95th percentile. Each dataset included 1600 training examples and 400 test images.

Due to the large image matrix size in the data, which was 640x372 (640x320) pixels for knee (brain) data, we were unable to fit more than 3-4 network unrolls on GPUs. To obtain high-quality competitive results, we reduced the data size as described next. To avoid conducting any data crimes [31], we provide a full description of the data preparation pipeline.

We computed the coil sensitivity maps using ESPIRiT and the BART toolbox [49, 50], with a calibration region of 20×20 (21×21) for the knee (brain) data. Then, ground-truth single-coil datasets were generated using the standard coil combination method: $x = \sum_{i=1}^{n_{coils}} S_i^* X_i$ where S_i is the sensitivity map of coil i . Note that this maintains the complex-valued nature of the data. Next, the coil-combined images were cropped in the image domain to 400×300 (320×230) pixels for the knee (brain) data. This cropping mainly removed background areas. Only the training examples were cropped. The inference samples were not cropped, to simulate realistic clinical scans. Because the network architecture is fully convolutional, inference can be done on images of any size.

4.2 Sampling

Terminology. Because k -band involves two different sampling schemes, we first explain our terminology. As mentioned above, the training data are acquired in bands. We use R_{band} to designate the scan time reduction achieved by this acquisition, compared with that of full k -space sampling. R_{band} is therefore the full k -space size over the band size, and $1/R_{band}$ is the relative band width. Additionally, we use R_{vd} to designate the acceleration obtained by the VD undersampling. It is worth noting that during training the VD sampling is applied only to the bands data, while during inference it is applied to the entire k -space.

Bands acquisition simulation. For training, we simulated bands acquisition using the coil-combined data described above. First, we computed the k -space of the complex-valued coil-combined cropped images, and then multiplied it by *binary band masks* with an orientation (angle) that was chosen randomly for each scan, from a range of $[0, 180]$ degrees with a uniform distribution (Fig 3, top row). These masks contain ones inside the band and zeros outside it. To keep R_{band} constant across all slices, the band width was varied with the angle, i.e. bands that were closer to a horizontal orientation were slightly wider than bands closer to a vertical orientation (Fig. 3, top). A new band mask was randomly generated for every k -space slice, to simulate realistic acquisition. We generated those masks only once, before the training, and saved them together with the k -space data. This avoids sampling multiple bands from the same slice in different training iterations and hence avoids "data crimes" [31]. Full implementation details can be found in our code <https://github.com/mikgroup/K-band>.

VD sampling. We conducted experiments using 1D and 2D VD schemes, as shown in Fig. 3. The VD masks were generated using SigPy [51]. Importantly, to maintain the VD statistics across all the examples in the training and test sets, the VD masks were first generated for the entire k -space area and then multiplied with the band masks, to generate the training data.

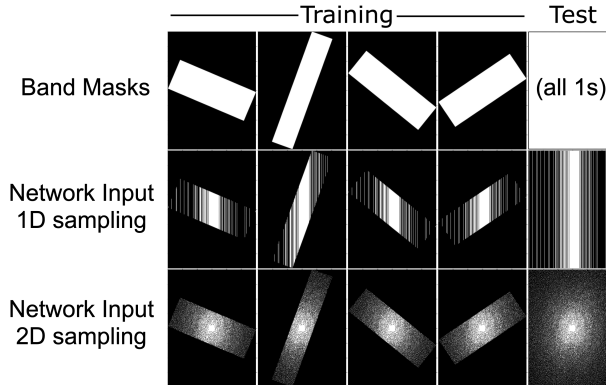


Figure 3: (Top) Visualization of supervision mask used during loss (with different angles) (Middle) 1D Poisson disc undersampling mask used for input to the network (Bottom) 2D Poisson disc undersampling mask used for input to the network.

4.3 Network implementation

The proposed k -band framework is agnostic to the network architecture, i.e. it can be implemented in different ways. Here we used the MoDL [24] implementation available in the DeepInPy toolbox [52]. This architecture includes a ResNet consisting of 64 hidden channels and 3×3 kernels. Following the steps described above for data size reduction, our networks included 7 unrolls and 6 ResNet blocks for the brain data, and 10 unrolls and 8 ResNet blocks for the knee data. We tuned the learning rate in a series of runs where the undersampling factors were set to $R_{band} = 4$ and $R_{vd} = 4$. All of our experiments were done with TITAN Xp, Titan X (Pascal), and NVIDIA GeForce RTX 3090

GPUs. To calibrate the learning rate, a grid search was done in the range of $1e^{-6}$ to $1e^{-3}$; a learning rate of $1e^{-4}$ was found to be best for *k*-band and all the other methods described next.

4.4 Comparison with other methods

We compared *k*-band with four other methods. The first two are trained using high-resolution data. Those are MoDL [24], which is fully supervised, i.e. trained with fully sampled *k*-space data, and SSDU [38] which is a SoTA self-supervised method, trained with under-sampled *k*-space data. However, because SSDU’s sampling mask covers the entire *k*-space, this method is also trained with high-resolution data. Note that *k*-space data can be undersampled but still have high resolution, as in SSDU, or be fully sampled but have limited/low resolution, as in *k*-band. We used the SSDU public GitHub code [38], [53], with the hyperparameters suggested by the authors. Specifically, the ratio of *k*-space samples used for data consistency vs. loss calculation was $\rho = 0.4$.

We also examined two self-supervised methods trained using only limited-resolution data. One of them, which we term “*k*-square”, is trained using only low-resolution data acquired in a square around *k*-space center (Fig. 4). This method was proposed in the SSDU paper as a benchmark. The other method, dubbed “*k*-vertical”, is trained using data from a *k*-space band that has a fixed vertical orientation in *k*-space (Fig. 4). This acquisition strategy was suggested in [54]. The *k*-square and *k*-vertical methods were both trained in a self-supervised manner, similar to *k*-band: the input to those networks was data from the square/vertical band, undersampled retrospectively using a VD mask, and supervision was done using all the data in the band.

We have taken careful steps to ensure a fair comparison of the above methods. First, all the self-supervised methods examined here (*k*-band, SSDU, *k*-square, and *k*-vertical) were trained using the same amount of data (MoDL is different because it uses full *k*-space data). Note that R_{vd} determines the amount of data that SSDU uses for supervision, and R_{band} determines the amount of data that *k*-band, *k*-vertical, and *k*-square use for supervision. In the experiments that compared them we therefore set $R_{vd} = R_{band}$, and then computed the band size for each method separately. Secondly, during inference all the five methods (MoDL and the four self-supervised methods) received the same type of data, VD-undersampled *k*-space, where the VD mask covered the entire *k*-space area (Fig 3, middle-right and bottom-right). These methods thus differed only in their training strategies. Third, the five methods were all implemented with the unrolled network architecture described above. Moreover, to ensure their optimal performance, the hyper-parameters were tuned for each method separately. The methods were evaluated by computing the Normalized Mean Square Error (NMSE), Structural Similarity Index Measure (SSIM) [55] and Peak Signal to Noise Ratio (PSNR) using the magnitude of the reconstructed and ground-truth images.

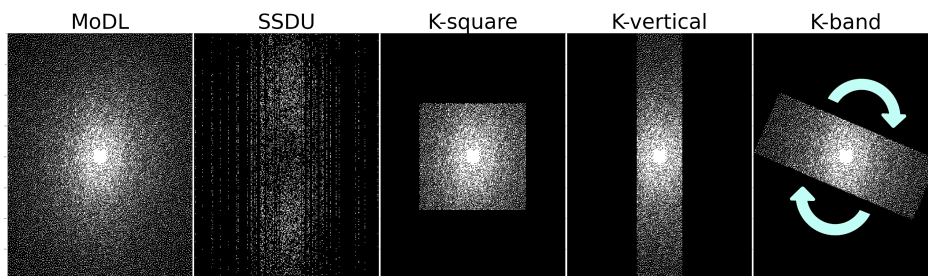
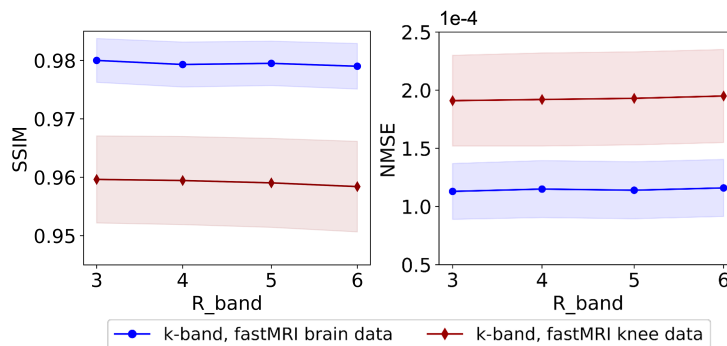


Figure 4: Sampling masks used for the five methods discussed in this work. In these examples $R_{band} = R_{vd} = 4$.

4.5 Loss functions

To investigate the use of different loss functions we performed experiments in which *k*-band and MoDL were trained using the fastMRI knee database. For *k*-band, we compared ℓ_1 and ℓ_2 *k*-space loss functions, both implemented with the weighting described above, and observed that ℓ_1 provided better results (Table 1). For MoDL we compared an image-domain ℓ_2 loss and ℓ_1 *k*-space loss, and observed better performance for the latter, similarly to [38] (Table 1). We thus use ℓ_1 *k*-space loss for both *k*-band and MoDL. SSDU was trained using the mixed ℓ_1/ℓ_2 loss suggested by its authors. Additionally, *k*-square and *k*-vertical were trained using ℓ_1 *k*-space loss, for a fair comparison with *k*-band.

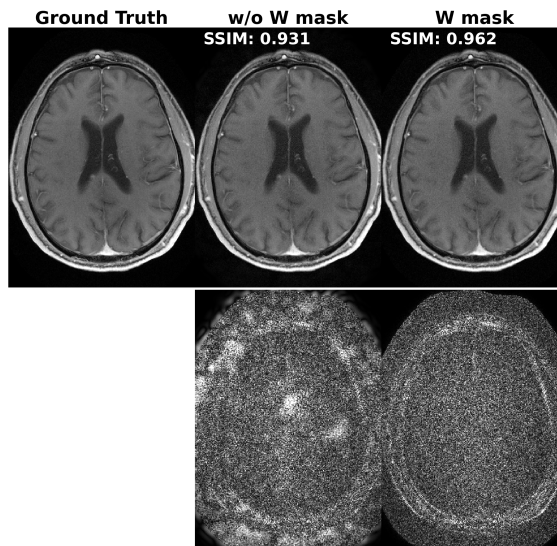
Error Metric	SSIM	NMSE	PSNR
K-band (k -space ℓ_1 loss)	0.959 ± 0.015	0.00019 ± 0.00008	40.40 ± 2.67
K-band (k -space ℓ_2 loss)	0.887 ± 0.037	0.00050 ± 0.00022	37.28 ± 2.80
MoDL (k -space ℓ_1 loss)	0.956 ± 0.016	0.00018 ± 0.00008	40.70 ± 2.70
MoDL (image ℓ_2 loss)	0.933 ± 0.023	0.00029 ± 0.00012	38.17 ± 2.73

Table 1: Comparison of loss functions for k -band and MoDL with $R_{vd} = R_{band} = 4$.Figure 5: Evaluation of k -band for a range of R_{band} (and $R_{vd} = 4$ fixed) using the fastMRI knee (blue) and brain (red) datasets. Note that k -band exhibits highly stable performance across a wide range of sampling parameters for the training data (left-to-right).

5 Results

5.1 Stability over varying band sizes

In the first experiment, k -band was trained using four different versions of the knee database, with varying band widths. Here, R_{band} was varied from 3 to 6; this corresponds to sampling approximately 33% to 16% of k -space. We did not test higher R_{band} values, i.e. extremely thin bands, because we used a fully-sampled calibration area for computing the sensitivity maps. To examine the reconstruction quality with respect to R_{band} alone, the VD acceleration was held constant at $R_{vd} = 4$. This experiment employed 2D VD undersampling. The results (Fig. 5) are that the SSIM and NMSE curves remained almost flat. This demonstrate that k -band exhibits high performance stability over a range of band sizes.

Figure 6: K -band results when trained with and without the loss-weighting (W) mask. Error maps, magnified by 10-fold, are shown below each reconstruction. Note that using the W mask leads to lower errors.

5.2 Loss weighting

To investigate the effect of the proposed W mask, we trained *k*-band with and without the mask. The experiments were conducted with $R_{band} = 3$ and $R_{vd} = 4$ using the brain data. The mean SSIM values were 0.964 ± 0.013 without the mask, and 0.980 ± 0.008 when the mask was used. A reconstruction example is shown in Fig. 6. These results suggest that training *k*-band with the W mask leads to overall sharper images.

5.3 Comparison to state-of-the-art methods

The five methods were compared by training them with undersampling factors of $R_{vd} = R_{band}$, which varied from 4 to 8. Experiments were done using the knee and brain data with 2D VD undersampling. The results shown in Fig. 7 (left column) and Fig. 8 indicate that *k*-band performs substantially better than the two other methods trained on limited-resolution data (*k*-vertical and *k*-square), and comparably to the methods trained on high-resolution data (SSDU and MoDL). Furthermore, the reconstructed images displayed in Fig. 9 and Fig. 10 (top) suggest that *k*-band obtains a visual quality similar to MoDL and SSDU, with the benefit of using only limited-resolution training data.

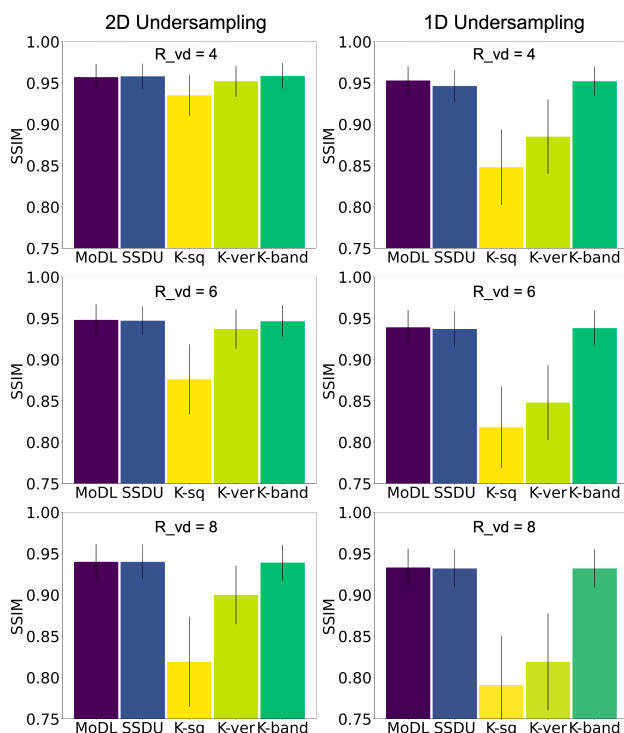


Figure 7: Comparison using the FastMRI knee data with both 2D and 1D VD undersampling during inference and $R_{vd} = R_{band} = 4, 6, 8$. Note that *k*-band performs comparably to SSDU and MoDL, with the advantage of being trained using only limited-resolution data.

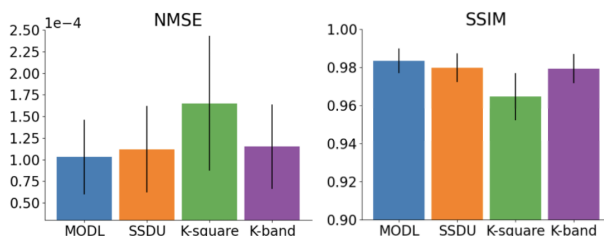


Figure 8: Comparison of *k*-band with the other methods using the FastMRI brain data, 2D VD undersampling and $R_{vd} = R_{band} = 4$. Note that *k*-band performs comparably to SSDU and MoDL, although it is trained only with limited-resolution data.

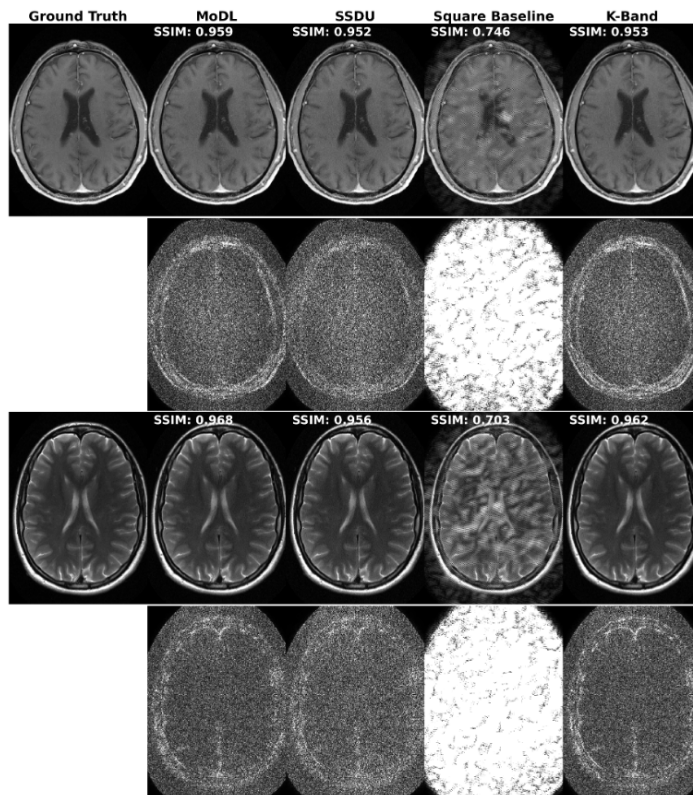


Figure 9: Reconstruction of the brain data with $R_{band} = 4, R_{vd} = 6$. *K*-band achieves better performance than *k*-square and comparable performance to MoDL and SSDU, even though it was trained using only limited-resolution data. Error maps are magnified by 14x.

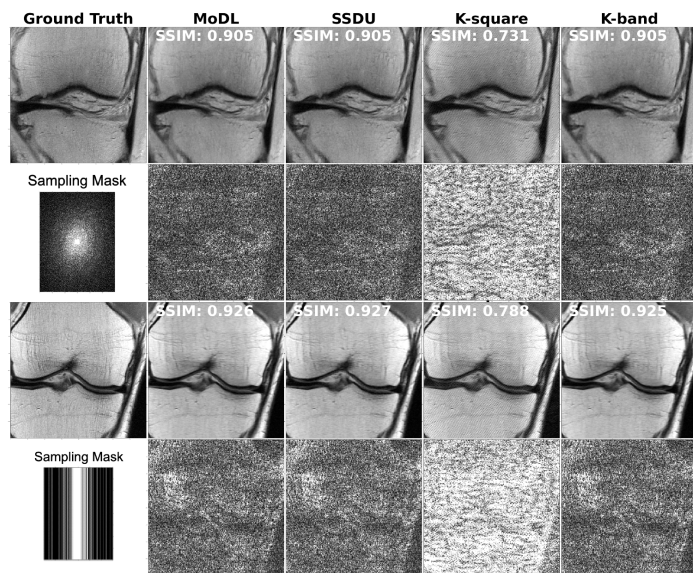


Figure 10: Examples for knee images reconstructed using MoDL, SSDU, and *k*-band, all trained with $R_{vd} = 8$. For *k*-band, the band width was $R_{band} = 8$. Experiments were done with 2D (top) and 1D (bottom) undersampling. Error maps, magnified by 10-fold, are shown below each reconstruction. Note that *k*-band performs comparably to the other methods although it was trained using only limited-resolution data.

We also trained the five methods using 1D VD undersampling masks. Note that 1D undersampling was not explored in the SSDU paper [38], so this can be viewed as a further analysis of this method. The statistical results presented in Fig. 7 (right column) indicate that k -band performs comparably to MoDL and SSDU in this regime, with slightly better performance than SSDU for $R_{vd} = 4$. The reconstructed images shown in Fig. 10 (bottom) also indicate that k -band obtains similar performance to MoDL and SSDU.

6 Discussion

Acquisition of fully-sampled data is challenging and quite impractical in high-dimensional (e.g. dynamic/volumetric) MRI. This is a barrier to the development of DL reconstruction methods, as those commonly require high-quality training data. To address these challenges, we introduce the k -band framework, which involves co-design of the acquisition and training strategies. We propose the concept of *SGD over k -space subsets*, where during training the gradients are computed using only k -space bands, which can be acquired efficiently. We derive the method analytically and find two simple conditions under which it stochastically approximates the desired (but impractical) SGD with fully sampled k -space data. Those correspond to randomization of the band orientation across scans and the use of a deterministic loss-weighting mask. We also demonstrate k -band in an extensive set of numerical experiments. Our results indicate that k -band obtains SoTA performance and high implementation stability, with the benefit of using only limited-resolution data.

The main merit in this study is the introduction of a framework that enables training networks using only datasets that were acquired with reduced resolution in one dimension. This approach can be particularly advantageous for dynamic MRI, where there is an inherent tradeoff between the spatial and temporal resolutions. Reducing the spatial resolution can enable faster data sampling, which is beneficial for many applications, e.g., cardiac [9, 25], Dynamic Contrast Enhanced [35], pulmonary [33], and 4D flow [34]. Moreover, as the scarcity of open-access raw MRI databases is a current bottleneck hindering the development of DL reconstruction techniques, the proposed strategy can pave the way towards easier creation of new databases.

Another important advantage of k -band is that its acquisition strategy can be implemented easily with numerous standard Cartesian MRI pulse sequences, which are the workhorses of clinical MRI. Notably, k -band can be implemented without any special preparations, by simply limiting the resolution along the PE dimension and changing the scan orientation; this is possible on any standard MRI scanner. Moreover, k -band is compatible with both 2D and 3D MRI acquisitions, as bands can be sampled either in planes or in a 3D volume.

Our results demonstrate that k -band offers high stability across a range of band widths (characterized by $1/R_{band}$) (Fig. 5) and acceleration factors (R_{vd}) (Fig. 7). Furthermore, the results indicate that use of the proposed loss-weighting mask improves the performance. The reason is that the loss weighting penalizes reconstruction errors in high-frequency areas more heavily than in the k -space center, thus compensating for the reduced exposure of the network to high-frequency areas during training.

We compared k -band with four other methods, all implemented with the same network architecture. Two of them, MoDL [24] and SSDU [38], are trained using high-resolution data. Note that although SSDU uses only subsampled measurements, their resolution is not reduced by the undersampling. In contrast, k -band is trained using data with limited resolution. The other two methods, k -square and k -vertical, are trained on limited-resolution data, with different band shapes and orientations. During inference, however, all five methods were evaluated using VD masks that cover the whole k -space. Our results indicate that k -band performs substantially better than the two other methods trained on low-resolution data, and comparably to MoDL and SSDU, yielding highly similar results both visually and quantitatively (Figs. 7 and 10). k -band hence achieves SoTA performance while also reducing the need for acquisition of high-resolution data.

The k -band method shares some similarity with the SSDU and SelfCoLearn [39] methods, as all three methods use only undersampled data and self-supervised training. However, both SSDU and SelfCoLearn assume that the undersampling mask covers all of k -space area, i.e. that the training data has a high resolution. In contrast, k -band assumes that the training data are acquired only within a band, thus enabling efficient data acquisition.

Furthermore, the loss-weighting method introduced here exhibits similarities to the approach proposed by Aggarwal et al [56]. They suggested loss weighting based on Stein’s unbiased estimator for the unsupervised training of DL reconstruction algorithms. However Stein’s unbiased estimator [57] makes stronger assumptions than unsupervised losses based on noise2noise [58], as the method considered in this paper.

This work also has some limitations. The proposed method was validated using the fastMRI database [27], i.e. using retrospective simulations with Cartesian data. Furthermore, although our code is suitable for multi-coil data, our

networks were trained on coil-combined data due to computational constraints. Future work will include validation of the method on prospectively acquired multi-coil data.

7 Conclusion

We introduced k -band, an acquisition-reconstruction framework that enables training self-supervised DL models using only limited-resolution data, with test-time generalization to high-resolution data. This work introduced the concept of SGD over k -space subsets, which is highly beneficial for training DL models in data-challenging regimes such as high-dimensional MRI. Our framework offers a practical solution, which enables rapid and easy data acquisition using any commercial MRI scanner. Numerical experiments demonstrate that k -band produces SoTA results, competitive with those of supervised and self-supervised techniques trained on high-resolution data, while also reducing the need for acquisition of such data. This work can hence pave the way towards development of new DL techniques for high-dimensional MRI.

References

- [1] K. P. Pruessmann, M. Weiger, M. B. Scheidegger, and P. Boesiger, “SENSE: sensitivity encoding for fast MRI,” *Magnetic Resonance in Medicine*, vol. 42, no. 5, pp. 952–962, 1999.
- [2] A. Deshmane, V. Gulani, M. A. Griswold, and N. Seiberlich, “Parallel MR imaging,” *Journal of Magnetic Resonance Imaging*, vol. 36, no. 1, pp. 55–72, 2012.
- [3] M. A. Griswold *et al.*, “Generalized autocalibrating partially parallel acquisitions (GRAPPA),” *Magnetic Resonance in Medicine*, vol. 47, no. 6, pp. 1202–1210, 2002.
- [4] M. Lustig and J. M. Pauly, “SPIRiT: iterative self-consistent parallel imaging reconstruction from arbitrary k -space,” *Magnetic Resonance in Medicine*, vol. 64, no. 2, pp. 457–471, 2010.
- [5] E. Shimron, A. G. Webb, and H. Azhari, “CORE-PI: Non-iterative convolution-based reconstruction for parallel MRI in the wavelet domain,” *Medical Physics*, vol. 46, no. 1, pp. 199–214, 2019.
- [6] M. Lustig, D. Donoho, and J. M. Pauly, “Sparse MRI: The application of compressed sensing for rapid MR imaging,” *Magnetic Resonance in Medicine*, vol. 58, no. 6, pp. 1182–1195, 2007.
- [7] M. Lustig, M. Alley, S. Vasanawala, D. L. Donoho, and J. M. Pauly, “L1 SPIR-iT: Autocalibrating parallel imaging compressed sensing,” in *Proc. Intl. Soc. Mag. Reson. Med.*, vol. 17, 2009, p. 379.
- [8] S. Vasanawala *et al.*, “Practical parallel imaging compressed sensing MRI: Summary of two years of experience in accelerating body MRI of pediatric patients,” in *2011 IEEE International Symposium on Biomedical Imaging*. IEEE, 2011, pp. 1039–1043.
- [9] M. Usman *et al.*, “Motion corrected compressed sensing for free-breathing dynamic cardiac MRI,” *Magnetic Resonance in Medicine*, vol. 70, no. 2, pp. 504–516, 2013.
- [10] L. Feng, L. Axel, H. Chandarana, K. T. Block, D. K. Sodickson, and R. Otazo, “XD-GRASP: golden-angle radial MRI with reconstruction of extra motion-state dimensions using compressed sensing,” *Magnetic Resonance in Medicine*, vol. 75, no. 2, pp. 775–788, 2016.
- [11] L. Feng, T. Benkert, K. T. Block, D. K. Sodickson, R. Otazo, and H. Chandarana, “Compressed sensing for body MRI,” *Journal of Magnetic Resonance Imaging*, vol. 45, no. 4, pp. 966–987, 2017.
- [12] E. Shimron, W. Grissom, and H. Azhari, “Temporal differences (TED) compressed sensing: a method for fast MRgHIFU temperature imaging,” *NMR in Biomedicine*, vol. 33, no. 9, p. e4352, 2020.
- [13] A. S. Lundervold and A. Lundervold, “An overview of deep learning in medical imaging focusing on MRI,” *Zeitschrift für Medizinische Physik*, vol. 29, no. 2, pp. 102–127, 2019.
- [14] C. M. Sandino, J. Y. Cheng, F. Chen, M. Mardani, J. M. Pauly, and S. S. Vasanawala, “Compressed sensing: From research to clinical practice with deep neural networks: Shortening scan times for magnetic resonance imaging,” *IEEE Signal Processing Magazine*, vol. 37, no. 1, pp. 117–127, 2020.
- [15] F. Knoll *et al.*, “Deep-learning methods for parallel magnetic resonance imaging reconstruction: A survey of the current approaches, trends, and issues,” *IEEE Signal Processing Magazine*, vol. 37, no. 1, pp. 128–140, 2020.
- [16] Y. Chen *et al.*, “AI-based reconstruction for fast MRI—a systematic review and meta-analysis,” *Proceedings of the IEEE*, vol. 110, no. 2, pp. 224–245, 2022.
- [17] K. Hammernik *et al.*, “Physics-Driven Deep Learning for Computational Magnetic Resonance Imaging,” *IEEE Signal Processing Magazine*, 2022.

- [18] S. Ravishankar, J. C. Ye, and J. A. Fessler, “Image reconstruction: From sparsity to data-adaptive methods and machine learning,” *Proceedings of the IEEE*, vol. 108, no. 1, pp. 86–109, 2019.
- [19] S. Wang *et al.*, “Accelerating magnetic resonance imaging via deep learning,” in *2016 IEEE International Symposium on Biomedical Imaging*, 2016, pp. 514–517.
- [20] D. Lee, J. Yoo, S. Tak, and J. C. Ye, “Deep residual learning for accelerated MRI using magnitude and phase networks,” *IEEE Transactions on Biomedical Engineering*, vol. 65, no. 9, pp. 1985–1995, 2018.
- [21] M. Akçakaya, S. Moeller, S. Weingärtner, and K. Uğurbil, “Scan-specific robust artificial-neural-networks for k -space interpolation (RAKI) reconstruction: Database-free deep learning for fast imaging,” *Magnetic Resonance in Medicine*, vol. 81, no. 1, pp. 439–453, 2019.
- [22] B. Zhu, J. Z. Liu, S. F. Cauley, B. R. Rosen, and M. S. Rosen, “Image reconstruction by domain-transform manifold learning,” *Nature*, vol. 555, no. 7697, pp. 487–492, 2018.
- [23] K. Hammernik *et al.*, “Learning a variational network for reconstruction of accelerated MRI data,” *Magnetic Resonance in Medicine*, vol. 79, no. 6, pp. 3055–3071, 2018.
- [24] H. K. Aggarwal, M. P. Mani, and M. Jacob, “MoDL: Model-based deep learning architecture for inverse problems,” *IEEE Transactions on Medical Imaging*, vol. 38, no. 2, pp. 394–405, 2018.
- [25] J. Schlemper, J. Caballero, J. V. Hajnal, A. Price, and D. Rueckert, “A deep cascade of convolutional neural networks for MR image reconstruction,” in *International Conference on Information Processing in Medical Imaging*. Springer, 2017, pp. 647–658.
- [26] J. Sun, H. Li, and Z. Xu, “Deep ADMM-Net for compressive sensing MRI,” *Advances in Neural Information Processing Systems*, vol. 29, 2016.
- [27] F. Knoll *et al.*, “fastMRI: A publicly available raw k -space and DICOM dataset of knee images for accelerated MR image reconstruction using machine learning,” *Radiology: Artificial Intelligence*, vol. 2, no. 1, 2020.
- [28] F. Ong, S. Amin, S. Vasanaawala, and M. Lustig, “Mridata.org: An open archive for sharing MRI raw data,” in *Proc. Intl. Soc. Mag. Reson. Med*, vol. 26, 2018, p. 1.
- [29] “Calgary Campinas Public Dataset,” sites.google.com/view/calgary-campinas-dataset/mr-reconstruction-challenge, 2020, accessed: 2021-03-22. [Online]. Available: sites.google.com/view/calgary-campinas-dataset/mr-reconstruction-challenge
- [30] A. D. Desai *et al.*, “SKM-TEA: A Dataset for Accelerated MRI Reconstruction with Dense Image Labels for Quantitative Clinical Evaluation,” in *Thirty-fifth Conference on Neural Information Processing Systems Datasets and Benchmarks Track*, 2021.
- [31] E. Shimron, J. I. Tamir, K. Wang, and M. Lustig, “Implicit data crimes: Machine learning bias arising from misuse of public data,” *Proceedings of the National Academy of Sciences*, vol. 119, no. 13, p. e2117203119, 2022.
- [32] K. S. Nayak, Y. Lim, A. E. Campbell-Washburn, and J. Steeden, “Real-Time Magnetic Resonance Imaging,” *Journal of Magnetic Resonance Imaging*, vol. 55, no. 1, pp. 81–99, 2022.
- [33] W. Jiang *et al.*, “Motion robust high resolution 3D free-breathing pulmonary MRI using dynamic 3D image self-navigator,” *Magnetic Resonance in Medicine*, vol. 79, no. 6, pp. 2954–2967, 2018.
- [34] M. Markl, A. Frydrychowicz, S. Kozerke, M. Hope, and O. Wieben, “4D flow MRI,” *Journal of Magnetic Resonance Imaging*, vol. 36, no. 5, pp. 1015–1036, 2012.
- [35] T. Zhang *et al.*, “Fast pediatric 3D free-breathing abdominal dynamic contrast enhanced MRI with high spatiotemporal resolution,” *Journal of Magnetic Resonance Imaging*, vol. 41, no. 2, pp. 460–473, 2015.
- [36] F. Ong *et al.*, “Extreme MRI: Large-scale volumetric dynamic imaging from continuous non-gated acquisitions,” *Magnetic Resonance in Medicine*, vol. 84, no. 4, pp. 1763–1780, 2020.
- [37] M. Akçakaya, B. Yaman, H. Chung, and J. C. Ye, “Unsupervised Deep Learning Methods for Biological Image Reconstruction and Enhancement: An overview from a signal processing perspective,” *IEEE Signal Processing Magazine*, vol. 39, no. 2, pp. 28–44, 2022.
- [38] B. Yaman, S. A. H. Hosseini, S. Moeller, J. Ellermann, K. Ugurbil, and M. Akcakaya, “Self-Supervised Learning of Physics-Guided Reconstruction Neural Networks without Fully-Sampled Reference Data,” *Magnetic Resonance in Medicine*, vol. 84, no. 6, pp. 3172–3191, Dec 2020.
- [39] J. Zou *et al.*, “SelfCoLearn: Self-supervised collaborative learning for accelerating dynamic MR imaging,” *Bio-engineering*, vol. 9, no. 11, p. 650, 2022.

- [40] Y. Korkmaz, S. U. Dar, M. Yurt, M. Özbey, and T. Cukur, “Unsupervised MRI reconstruction via zero-shot learned adversarial transformers,” *IEEE Transactions on Medical Imaging*, 2022.
- [41] B. Yaman, S. A. H. Hosseini, and M. Akçakaya, “Zero-shot self-supervised learning for MRI reconstruction,” *International Conference on Learning Representations*, 2022.
- [42] J. Liu, Y. Sun, C. Eldeniz, W. Gan, H. An, and U. S. Kamilov, “Rare: Image reconstruction using deep priors learned without groundtruth,” *IEEE Journal of Selected Topics in Signal Processing*, vol. 14, no. 6, pp. 1088–1099, 2020.
- [43] K. Gong, P. Han, G. El Fakhri, C. Ma, and Q. Li, “Arterial spin labeling MR image denoising and reconstruction using unsupervised deep learning,” *NMR in Biomedicine*, vol. 35, no. 4, p. e4224, 2022.
- [44] M. Z. Darestani and R. Heckel, “Accelerated mri with un-trained neural networks,” *IEEE Transactions on Computational Imaging*, vol. 7, p. 724–733, 2021.
- [45] R. Heckel and P. Hand, “Deep decoder: Concise image representations from untrained non-convolutional networks,” in *International Conference on Learning Representations*, 2019.
- [46] E. K. Cole, J. M. Pauly, S. S. Vasanawala, and F. Ong, “Unsupervised MRI reconstruction with generative adversarial networks,” *arXiv preprint arXiv:2008.13065*, 2020.
- [47] M. J. Muckley, B. Riemenschneider, A. Radmanesh, S. Kim, G. Jeong, J. Ko, Y. Jun, H. Shin, D. Hwang, M. Mostapha *et al.*, “Results of the 2020 fastmri challenge for machine learning mr image reconstruction,” *IEEE transactions on medical imaging*, vol. 40, no. 9, pp. 2306–2317, 2021.
- [48] T. Klug, D. Atik, and R. Heckel, “Analyzing the sample complexity of self-supervised image reconstruction methods,” May 2023, arXiv:2305.19079 [cs, eess].
- [49] M. Uecker *et al.*, “ESPIRiT—an eigenvalue approach to autocalibrating parallel MRI: where SENSE meets GRAPPA,” *Magnetic Resonance in Medicine*, vol. 71, no. 3, pp. 990–1001, 2014.
- [50] M. Uecker, F. Ong, J. I. Tamir, D. Bahri, P. Virtue, J. Y. Cheng, T. Zhang, and M. Lustig, “Berkeley advanced reconstruction toolbox,” in *Proc. Intl. Soc. Mag. Reson. Med.*, vol. 23, no. 2486, 2015.
- [51] F. Ong and M. Lustig, “SigPy: a python package for high performance iterative reconstruction,” in *Proc. Intl. Soc. Mag. Reson. Med.*, vol. 4819, 2019.
- [52] J. I. Tamir, S. X. Yu, and M. Lustig, “DeepInPy: Deep Inverse Problems in Python,” in *ISMRM Workshop on Data Sampling and Image Reconstruction*, 2020.
- [53] Yaman, Burhaneddin and Hosseini, Seyed Amir Hossein and Moeller, Steen and Ellermann, Jutta and Ugurbil, Kamil and Akcakaya, Mehmet, “Self-supervised physics-based deep learning MRI reconstruction without fully-sampled data,” in *Proc. IEEE Int. Symp. Biomed. Imag. (ISBI)*. IEEE, 2020, pp. 921–925.
- [54] M. Mayberg *et al.*, “Anisotropic neural deblurring for MRI acceleration,” *International Journal of Computer Assisted Radiology and Surgery*, vol. 17, no. 2, pp. 315–327, 2022.
- [55] Z. Wang, A. C. Bovik, H. R. Sheikh, and E. P. Simoncelli, “Image quality assessment: from error visibility to structural similarity,” *IEEE Transactions on Image Processing*, vol. 13, no. 4, pp. 600–612, 2004.
- [56] H. K. Aggarwal, A. Pramanik, and M. Jacob, “Ensure: Ensemble stein’s unbiased risk estimator for unsupervised learning,” in *ICASSP 2021-2021 IEEE International Conference on Acoustics, Speech and Signal Processing (ICASSP)*. IEEE, 2021, pp. 1160–1164.
- [57] C. A. Metzler, A. Mousavi, R. Heckel, and R. G. Baraniuk, “Unsupervised learning with stein’s unbiased risk estimator,” *arXiv preprint arXiv:1805.10531*, 2018.
- [58] J. Lehtinen, J. Munkberg, J. Hasselgren, S. Laine, T. Karras, M. Aittala, and T. Aila, “Noise2noise: Learning image restoration without clean data,” *arXiv preprint arXiv:1803.04189*, 2018.